

RAPID FLIGHT DYNAMICS EVALUATION OF STRONGLY COUPLED DISTRIBUTED PROPULSION

Yue Zhu[1,2], Rui Wang[1,2], Yuhang Xie[1,2], Zhou Zhou[1,2]

[1] School of Aeronautics, Northwestern Polytechnical University, Xi'an, 710129, China
[2] National Key Laboratory of Aircraft Configuration Design, Xi'an 710072, China

Abstract

Distributed-propulsion aircraft improve lift and low-speed performance through propulsion–wing aerodynamic coupling, but propeller slipstream alters local inflow and makes aerodynamic derivatives vary with propulsion state. Existing studies mainly address aerodynamic loads, thrust-induced moments, or control responses, while the influence of slipstream-induced derivative changes on aircraft dynamics remains insufficiently clarified. This paper proposes a rapid flight-dynamics evaluation method for conceptual design. Propeller slipstream is modeled using blade element momentum theory and introduced into the vortex lattice method. Stability, dynamic, and control derivatives under different propulsion states are extracted by finite-difference perturbation and incorporated into a derivative-corrected flight-dynamics model. A tandem-wing distributed-propulsion aircraft is analyzed. Results show that, at cruise angle of attack, slipstream increases lift coefficient by 60% and aileron effectiveness by 168%, increases longitudinal modal damping, and accelerates roll-mode convergence. The method agrees well with CFD results at small angles of attack.

Keywords: Distributed Electric Propulsion, Flight Dynamics, Slipstream Effects, BEMT, VLM

1. Introduction

Distributed electric propulsion (DEP) aircraft arrange multiple propulsion units along the wing or fuselage, enabling deep integration between the propulsion system and the aerodynamic configuration. This arrangement offers clear advantages in increasing lift coefficient, improving low-speed performance, delaying stall, and enhancing control authority [1-4]. However, distributed-propulsion slipstream changes the local inflow conditions of the wing and control surfaces, causing aerodynamic forces, moments, and their derivatives with respect to state and control variables to vary with propulsion state. This produces pronounced aero-propulsive-control coupling characteristics.

Current research on the aerodynamic characteristics of distributed-propulsion aircraft is mostly based on computational fluid dynamics (CFD). Because CFD is computationally expensive and time-consuming, these studies usually focus on basic lift-drag characteristics and lift-enhancement effects, and have shown that distributed-propulsion aircraft can significantly improve aerodynamic performance [5-8]. In flight-dynamics modeling and stability-and-control analysis, Vechtel and Buch estimated dynamic derivatives using empirical formulas and analyzed the influence of configuration parameters on the Dutch-roll mode for overall configuration optimization, but did not fully consider the propulsion-system correction to aerodynamic derivatives [9]. He et al. established a slipstream-effect model using XROTOR coupled with a vortex lattice method and applied it to model predictive control for power yaw of a DEP aircraft, confirming the importance of slipstream modeling for power-yaw control performance [10], but the dynamic-response changes caused by distributed propulsion were

not considered. In control-law design for power yaw, several studies have investigated aircraft dynamic characteristics, usually using aerodynamic analysis software based on the vortex lattice method to calculate dynamic and control derivatives and establish dynamic models [11-14]. However, such methods are mostly based on conventional aerodynamic configurations or derivative calculations under no-slipstream conditions, and therefore cannot fully capture the influence of distributed-propulsion slipstream on aerodynamic derivatives. Botta and Cacciola modeled aero-propulsive coupling effects by combining results at discrete advance ratios with system identification within a classical stability- and control-derivative framework [15, 16]. Geng et al. [17] developed a nonlinear dynamic model for a turboprop aircraft under strong slipstream effects to study lateral-directional responses under crosswind and one-engine-inoperative conditions, but did not provide specific dynamic-derivative data or the way in which they were obtained. In addition, MIT manufactured a flight demonstrator and conducted flight tests, identifying the maximum lift coefficient from flight data and analyzing handling qualities [18].

In summary, existing studies have explored the aerodynamic and control characteristics of distributed-propulsion aircraft from the perspectives of CFD simulation, empirical estimation, aerodynamic-software modeling, system identification, and flight testing. However, for aerodynamic derivatives under slipstream effects, especially the variation of dynamic derivatives and their influence on the aircraft body flight dynamics, a modeling and analysis method that combines computational efficiency with physical interpretability is still lacking.

This paper proposes a rapid flight-dynamics evaluation method for distributed-propulsion aircraft in the conceptual design stage. First, the method establishes a propeller thrust and slipstream model based on blade element momentum theory (BEMT), and introduces the slipstream induced velocity into the vortex lattice method (VLM) for aerodynamic calculation, thereby obtaining the whole-aircraft aerodynamic forces and moments under different propulsion states. Then, a small-perturbation finite-difference method is used to extract stability derivatives, dynamic derivatives, and control derivatives, and a flight-dynamics model containing aero-propulsive coupling derivative corrections is established. Finally, a tandem-wing distributed-propulsion unmanned aerial vehicle is used as a case study to analyze the influence of slipstream on basic aerodynamic characteristics, key aerodynamic derivatives, control effectiveness, and typical modal characteristics. The proposed method is validated through comparison with CFD results and provides support for rapid stability-and-control evaluation of distributed-propulsion aircraft during conceptual design.

2. Rapid Computation Method for Distributed Propulsion/Aerodynamic Coupling

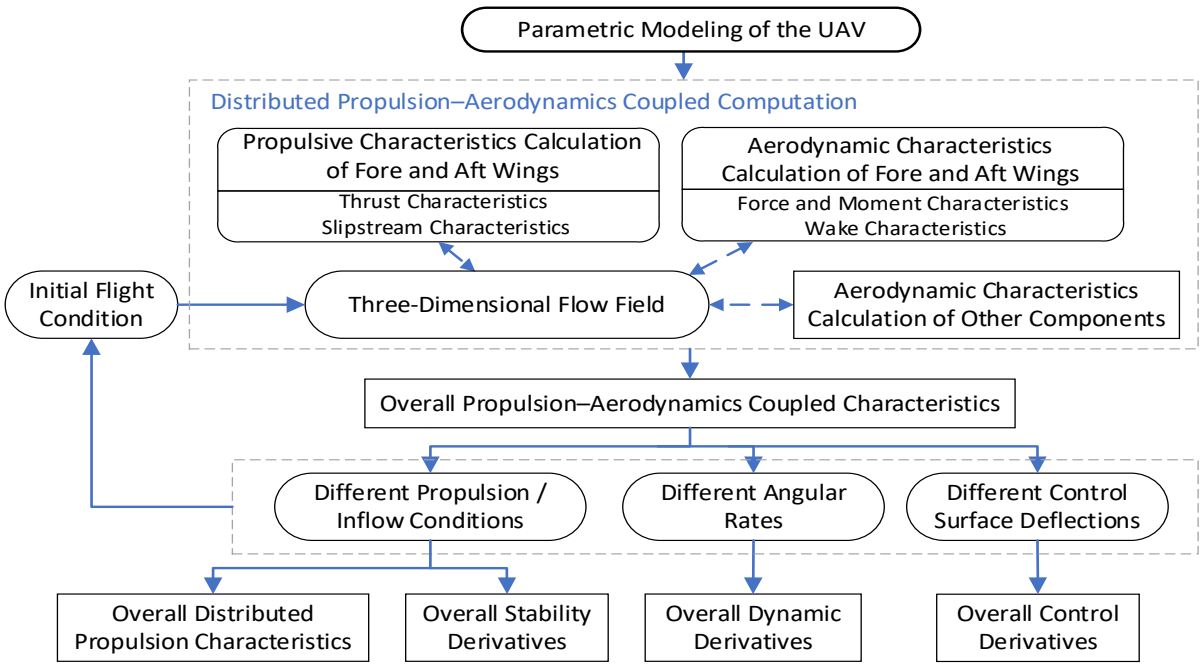


Figure 1 – Schematic of the Aero-Propulsive-Control Coupling Computational Procedure.

The rapid evaluation workflow for distributed propulsion/aerodynamics/flight-dynamics coupling proposed in this paper is shown in Figure 1. The workflow first uses BEMT to calculate propeller thrust

and slipstream induced velocity, and then introduces the slipstream velocity into the VLM aerodynamic calculation to obtain whole-aircraft aerodynamic forces and moments under different propulsion states. Perturbations in states, angular rates, and control inputs are then applied near the baseline condition to extract stability derivatives, dynamic derivatives, and control derivatives. Finally, the obtained aerodynamic derivatives are introduced into the flight-dynamics model for trim, modal, and control-response analysis. This section focuses on the BEMT-VLM aero-propulsive coupling calculation method; derivative extraction and flight-dynamics modeling are given in the next section.

2.1 BEMT-Based Propeller Thrust and Slipstream Model

Blade element momentum theory is used in this paper to solve the relevant propeller characteristics. According to momentum theory, the propeller thrust and torque are calculated as:

$$\begin{aligned} T_M &= 4\pi r \rho V_\infty^2 a(1+a)\delta r F \\ Q_M &= 4\pi r^3 \rho V_\infty^2 \omega a'(1+a)\delta r F \end{aligned} \tag{1}$$

where rho is the air density; V_∞ is the freestream velocity; F is the Prandtl tip-loss factor; r is the radial distance from the blade element to the blade rotation center; and a and a' are the axial and tangential induction factors, respectively, which are the core unknowns solved in the BEMT method.

According to blade element theory, the propeller thrust and torque are calculated as:

$$\begin{aligned} T_E &= 0.5\rho W^2 c(C_l \cos\phi + C_d \sin\phi) N \delta r \\ Q_E &= 0.5\rho W^2 c r(C_l \sin\phi + C_d \cos\phi) N \delta r \end{aligned} \tag{2}$$

where N is the number of blades; C_l and C_d are the lift and drag coefficients of the blade element, determined by the airfoil of the blade element; ϕ is the inflow angle, namely the angle between the incoming flow and the propeller rotation plane; c is the blade-element chord; and W is the resultant velocity at the propeller plane. By equating the thrust and torque calculated from momentum theory and blade element theory, the equilibrium equations at the blade element can be established:

$$\begin{cases} T_M - T_E = 0 \\ Q_M - Q_E = 0 \end{cases} \tag{3}$$

After the propeller geometry, flight altitude, freestream velocity, and rotational speed are specified, the induction factors a and a' can be obtained from the equations, and the propeller thrust, torque, and induced-velocity distribution can then be determined. Based on these results, a three-dimensional propeller slipstream field is further constructed to provide input for the subsequent distributed propulsion/aerodynamic coupling calculation.

2.2 VLM Aerodynamic Calculation Coupled with Slipstream Induced Velocity

The vortex lattice method is a low-order panel method based on potential-flow theory. Its basic idea is to use discrete horseshoe vortices to represent the disturbance of the wing and tail surfaces to the flow field, solve the circulation distribution by satisfying the no-penetration boundary condition at the control points, and then calculate aerodynamic characteristics such as lift, induced drag, and moments. On the basis of the conventional VLM, this paper introduces the propeller slipstream velocity calculated by BEMT and corrects the local inflow condition to represent the influence of distributed propulsion on wing aerodynamic characteristics.

In the calculation, the wing mean-camber surface is discretized into N rectangular panels. A horseshoe vortex is arranged on each panel, and the control point is placed at the midpoint of the panel chord line. According to the no-penetration boundary condition, the normal velocity at each control point is zero, and a linear system for the horseshoe-vortex circulation can be established:

$$\sum_{j=1}^{N} A_{ij}\Gamma_j + V_{\infty,n} = 0 \tag{4}$$

where i and j are vortex-lattice indices; A_{ij} is the influence coefficient, representing the normal induced velocity generated at the control point of the i-th panel by a unit circulation on the j-th vortex lattice, and can be expressed as:

$$A_{ij} = \vec{V}_{ij} \cdot \vec{n}_i \tag{5}$$

where v_{ij} is the unit-circulation induced velocity generated by the j-th horseshoe vortex at the i-th control point; n_i is the normal vector of the i-th vortex lattice; and $V_{\infty,n}$ is the projection of the freestream velocity in the normal direction at that control point, namely:

$$V_{\infty,n} = \vec{V}_{\infty} \cdot \vec{n}_i \tag{6}$$

When slipstream effects are considered, the freestream velocity is modified to the local inflow velocity after superposing the slipstream velocity, allowing the distributed-propulsion induced velocity to be introduced into the VLM calculation framework.

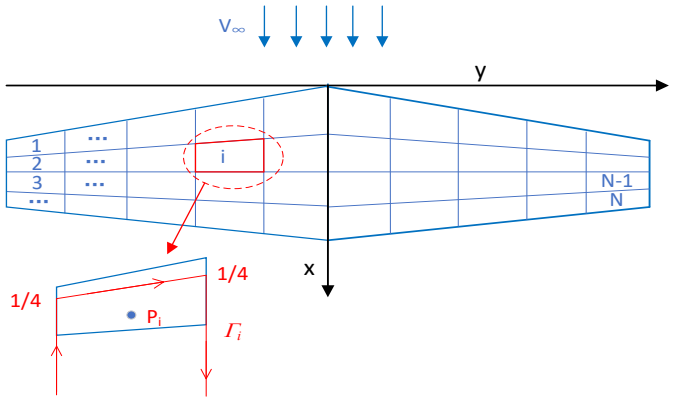


Figure 2 – Vortex lattice layout of wing.

After the circulation distribution is obtained, the aerodynamic force on each panel is calculated using the Kutta-Joukowski theorem:

$$\mathbf{F}_i = \rho \Gamma_i \mathbf{V}_{eff} \times \overrightarrow{(AB)}_i \tag{7}$$

where V_{eff} is the effective inflow velocity at the i-th vortex lattice; $\overrightarrow{AB}$ is the bound-vortex segment vector of that lattice; and Γ_i is the corresponding circulation. A downwash angle exists between the wake coordinate system and the wind-axis coordinate system, and is defined as:

$$\varepsilon = \tan^{-1}\left(\frac{V_{ind}}{V_{\infty}}\right) \tag{8}$$

where V_{ind} is the induced velocity of the wake on the Trefftz plane. Summing the aerodynamic forces over all vortex lattices yields the aerodynamic force of a single lifting surface. Superposing the results of all lifting surfaces then gives the whole-aircraft aerodynamic force. The whole-aircraft aerodynamic moment can be calculated from the moment arm between each vortex-lattice position and the moment reference point.

2.3 Validation of the Rapid Aero-Propulsive Coupling Calculation Method

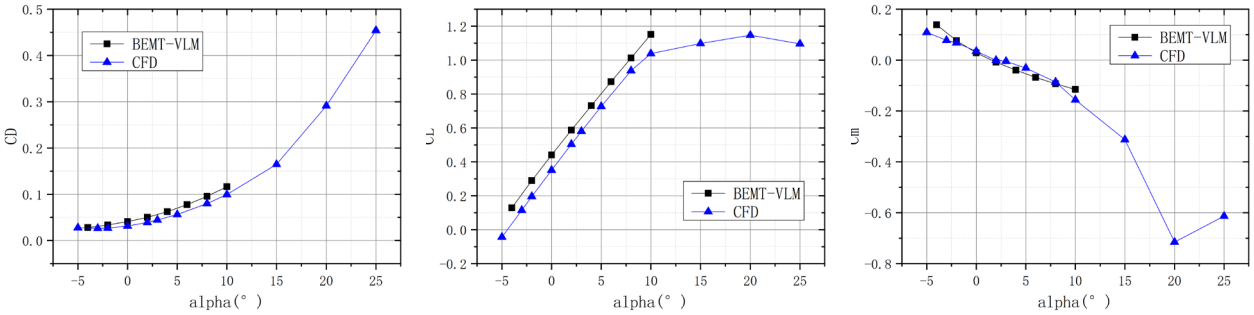


Figure 3 – Comparison between VLM and CFD results.

To validate the applicability of the low-order aerodynamic calculation method for subsequent derivative extraction, this paper first calculates the lift coefficient, induced-drag coefficient, and pitching-moment coefficient of the tandem-wing aircraft at different angles of attack under the no-slipstream baseline condition using both VLM and CFD. The results are shown in Figure 3. The comparison shows that, in the small-to-moderate angle-of-attack range, the lift-curve slope, drag-variation trend, and pitching-moment variation predicted by VLM are generally consistent with the CFD results, and the errors in the main aerodynamic coefficients remain within 10%. Because VLM is based on the potential-flow assumption, it is difficult to fully capture the zero-lift offset and large-angle-of-attack separation characteristics. Therefore, this method is mainly used in this paper for rapid aerodynamic-derivative

extraction and dynamic-trend analysis within the unstalled range.

3. Aerodynamic Derivative Calculation and Flight-Dynamics Modeling Under Aero-Propulsive Coupling

3.1 Calculation of Dynamic and Control Derivatives

Based on the BEMT-VLM aero-propulsive coupling calculation method established above, the whole-aircraft aerodynamic forces and moments can be obtained for a given flight state and propulsion state. To further establish the flight-dynamics model, small perturbations in state variables, angular-rate variables, and control variables are applied near the baseline condition, and a finite-difference method is used to calculate stability derivatives, dynamic derivatives, downwash time-lag derivatives, and control derivatives.

3.1.1 Dynamic derivatives

After the basic whole-aircraft aerodynamic characteristics under the baseline condition are obtained, small perturbations are applied to the attitude angular rates p, q, and r. Because aircraft rotation changes the local inflow velocity at each vortex lattice, the additional inflow caused by rotational motion must be calculated according to the vortex-lattice position. For the i-th vortex lattice with coordinates $\boldsymbol{P}_i = [x, y, z]^T$, the local inflow velocity considering aircraft rotation can be expressed as:

$$\mathbf{V}_{\infty,i} = \mathbf{V}_\infty + \boldsymbol{\Omega} \times \mathbf{P}_i \tag{9}$$

where： $\boldsymbol{\Omega} = [p, q, r]^T$ is the three-axis angular velocity about the center of gravity.

The local inflow velocity obtained from the equation is used as the new boundary condition, and VLM is again used to calculate the six-component aerodynamic forces and moments under the perturbed condition. By differencing these results from the baseline condition, the aircraft dynamic derivatives can be obtained. This method captures the influence of angular-rate perturbations on local inflow and whole-aircraft aerodynamic response, providing parameters for subsequent linearized dynamic modeling and modal-characteristic analysis.

3.1.2 Downwash time-lag derivatives

The downwash time-lag derivatives are mainly used to describe the unsteady influence of angle-of-attack rate on the local inflow of the rear wing. When the angle of attack of the front wing changes, the resulting downwash velocity does not act on the rear wing instantaneously, but has a certain propagation delay. Therefore, the key to calculating the downwash time-lag derivatives is to determine the equivalent local angle of attack and downwash-velocity variation at the rear wing under the action of the angle-of-attack rate.

Given a small angle-of-attack rate, the equivalent local angle of attack at the rear wing can be expressed as:

$$\alpha_{t_1} = \alpha - \dot{\alpha} \frac{l_h}{V_\infty} \tag{10}$$

where l_h is the distance from the front wing to the rear wing along the freestream direction; α is the baseline angle of attack; and α_{t_1} is the local rear-wing angle of attack after considering downwash time lag. Substituting the corrected local angle of attack and corresponding downwash condition into the VLM calculation model yields the whole-aircraft aerodynamic forces and moments after considering the downwash time-lag effect. Differencing these results from the baseline condition gives the downwash time-lag derivatives, such as $C_{L\dot{\alpha}}$ and $C_{m\dot{\alpha}}$. These derivatives reflect the influence of angle-of-attack rate on rear-wing aerodynamic response and whole-aircraft longitudinal unsteady aerodynamic moments.

3.1.3 Control derivatives

Control derivatives characterize the influence of control-surface deflection on whole-aircraft aerodynamic forces and moments. In the calculation, vortex lattices containing control surfaces are first identified during the lattice discretization. The corresponding control surface is then deflected by a small angle about its hinge line, and the geometric positions, normal vectors, and local inflow conditions of the control-surface vortex lattices are updated. VLM is then performed again on the updated vortex-lattice model to obtain the six-component aerodynamic forces and moments under the control-surface deflection condition. Differencing these results from the baseline condition yields the corresponding control derivatives.

3.2 Flight-Dynamics Equations with Distributed Propulsion/Aerodynamic Coupling

Based on the gravity, aerodynamic forces, and thrust acting on the aircraft, the nonlinear dynamic equations of the distributed-propulsion UAV are established. The dynamic and kinematic equations used are:

$$\begin{cases} m(\dot{V}+\Omega\times V)=\sum F \\ I\dot{\Omega}+\Omega\times(I\Omega)=\sum M \\ \dot{X}_g=L_{gb}V \\ \dot{\Psi}=L_{\Psi}\Omega \end{cases} \tag{11}$$

where $\mathbf{V}$, $\mathbf{\Omega}$, $\mathbf{X}_g$, and $\mathbf{\Psi}$ are the UAV linear velocity, angular velocity, position in the ground coordinate system, and Euler angles, respectively; m and I are the UAV mass and moment-of-inertia matrix, respectively; L_{gb} and L_{Ψ} are the coordinate transformation matrix from the body axis to the ground axis and the projection matrix from angular velocity to Euler-angle rates; and $\sum F$ and $\sum M$ are the resultant external force and resultant external moment of the aircraft. The resultant force and moment are expanded as:

$$\begin{cases} \sum F=L_{ba}F_A+\sum_{i=1}^{n_p}(L_{bp,i}T_i)+L_{bg}F_G \\ \sum M=L_{ba}M_A+\sum_{i=1}^{n_p}[R_{P,i}\times(L_{bp,i}T_i)+L_{bp,i}Q_{p,i}] \end{cases} \tag{12}$$

where F_A and M_A are the aerodynamic force and moment generated by the aerodynamic configuration; T and Q_P are the thrust or pulling force and reaction torque generated by the propulsion system; G is the UAV gravity; L_{ba}, L_{bg}, and L_{bp} are the transformation matrices from the wind-axis, ground, and propulsion-system coordinate systems to the body coordinate system, respectively; R_P is the coordinate of the propulsion-system origin in the UAV body coordinate system; n_P denotes the number of propulsion units in the distributed-propulsion system; and the subscript i denotes the i-th individual propulsion unit.

The aerodynamic forces and moments are expressed in the following nondimensional form:

$$F_A=\frac{1}{2}\rho V^2S\begin{bmatrix}-C_D\\ C_Y\\ -C_L\end{bmatrix},\quad M_A=\frac{1}{2}\rho V^2S\begin{bmatrix}bC_l\\ cC_m\\ bC_n\end{bmatrix} \tag{13}$$

where C_L, C_D, and C_Y are the lift, drag, and side-force coefficients of the UAV, respectively; C_l, C_m, and C_n are the roll, pitch, and yaw moment coefficients, respectively; ρ is the air density; V为 is the freestream velocity; and S, b, and c are the UAV reference area, span, and chord, respectively.

The nonlinear dynamic equations of the aircraft are further linearized based on small-perturbation linearization theory, and the longitudinal and lateral-directional linear dynamic equations are established separately. The longitudinal state-space equation is:

$$\dot{x}_{lon}=A_{lon}x_{lon}+B_{lon}u_{lon} \tag{14}$$

where:

$$\begin{aligned} x_{lon}&=[V,\alpha,q,\theta]^T \\ u_{lon}&=[\delta_e,\delta_{t,1}\cdots\delta_{t,n_p}]^T \\ A_{lon}&=\begin{bmatrix} X_V & X_\alpha+g & 0 & -g \\ -Z_V & -Z_\alpha & 1 & 0 \\ \bar{M}_V-\bar{M}_{\dot{\alpha}}Z_V & \bar{M}_\alpha-\bar{M}_{\dot{\alpha}}Z_\alpha & \bar{M}_q-\bar{M}_{\dot{\alpha}} & 0 \\ 0 & 0 & 1 & 0 \end{bmatrix} \\ B_{lon}&=\begin{bmatrix} X_{\delta_e} & X_{\delta_{t,1}} & \cdots & X_{\delta_{t,n_p}} \\ -Z_{\delta_e} & -Z_{\delta_{t,1}} & \cdots & -Z_{\delta_{t,n_p}} \\ \bar{M}_{\delta_e}-\bar{M}_{\dot{\alpha}}Z_{\delta_e} & \bar{M}_{\delta_{t,1}}-\bar{M}_{\dot{\alpha}}Z_{\delta_{t,1}} & \cdots & \bar{M}_{\delta_{t,n_p}}-\bar{M}_{\dot{\alpha}}Z_{\delta_{t,n_p}} \\ 0 & 0 & \cdots & 0 \end{bmatrix} \end{aligned} \tag{15}$$

The lateral-directional state-space equation is:

$$\dot{x}_{lat} = A_{lat} x_{lat} + B_{lat} u_{lat} \tag{16}$$

where:

$$\begin{aligned} x_{lat} &= [\beta, p, r, \phi]^T \\ u_{lat} &= [\delta_a, \delta_r, \delta_{t,1} \cdots \delta_{t,n_p}]^T \\ A_{lat} &= \begin{bmatrix} \overline{Y}_\beta & \alpha_0 + \overline{Y}_p & \overline{Y}_r - 1 & g\cos\theta_0 / V_0 \\ \overline{L}_\beta & \overline{L}_p & \overline{L}_r & 0 \\ \overline{N}_\beta & \overline{N}_p & \overline{N}_r & 0 \\ 0 & 1 & \tan\theta_0 & 0 \end{bmatrix} \\ B_{lat} &= \begin{bmatrix} \overline{Y}_{\delta_a} & \overline{Y}_{\delta_r} & 0 & \cdots & 0 \\ \overline{L}_{\delta_a} & \overline{L}_{\delta_r} & \overline{L}_{\delta_{t,1}} & \cdots & \overline{L}_{\delta_{t,n_p}} \\ \overline{N}_{\delta_a} & \overline{N}_{\delta_r} & \overline{N}_{\delta_{t,1}} & \cdots & \overline{N}_{\delta_{t,n_p}} \\ 0 & 0 & 0 & \cdots & 0 \end{bmatrix} \end{aligned} \tag{17}$$

Based on the above nonlinear dynamic model and its linearized form, the following analysis focuses on trim characteristics, stability, and controllability, with the goal of revealing the influence of distributed propulsion on the stability-and-control characteristics of the aircraft.

4. Case Study and Flight-Dynamics Characteristics Analysis

A tandem-wing aircraft is used as the case study for analysis and validation of the algorithm. The layout of the tandem-wing distributed-propulsion aircraft is shown in Figure 4. Four propellers are arranged on each of the front and rear wings, with the front wing lower than the rear wing. The overall UAV parameters are listed in Table 1.

Table 1 – General Parameters of the Case Study Aircraft.

Parameter	Value	Parameter	Value
Mass (kg)	9	Mean Aerodynamic Chord (m)	0.3
Cruise Angle of Attack (deg)	2	Front Wing Span (m)	2.2
Rear Wing Span (m)	2.6	Reference area (m^2)	1.396
I_{yy} ($kg*m^2$)	1.5	I_{xx} ($kg*m^2$)	1.8
I_{xz} ($kg*m^2$)	0.221	I_{zz} ($kg*m^2$)	3.18

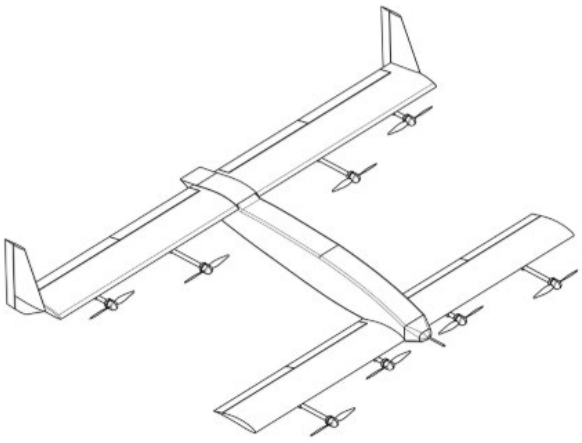


Figure 4 – Schematic of the Overall Layout of the Case Study Aircraft.

4.1 Basic Aerodynamic Characteristics Analysis

To evaluate the influence of distributed propulsion/aerodynamic coupling on the basic aerodynamic performance of the aircraft, sea-level altitude and a flight speed of $V = 10\ m/s$ are selected as the calculation condition. This speed is close to the minimum level-flight speed of the aircraft without propulsion, and therefore clearly reflects the enhancement of low-speed aerodynamic performance caused by propeller slipstream. Figure 5 gives the computed lift coefficient, induced-drag coefficient,

and pitching-moment coefficient of the whole aircraft as functions of angle of attack under different thrust coefficients. Here, C_t is the nondimensional thrust coefficient of the UAV, and its relationship with whole-aircraft thrust T and propeller thrust coefficient C_T is:

$$C_t = \frac{T}{0.5\rho V_\infty^2 S} = C_T \frac{2D^2}{J^2 S} \tag{18}$$

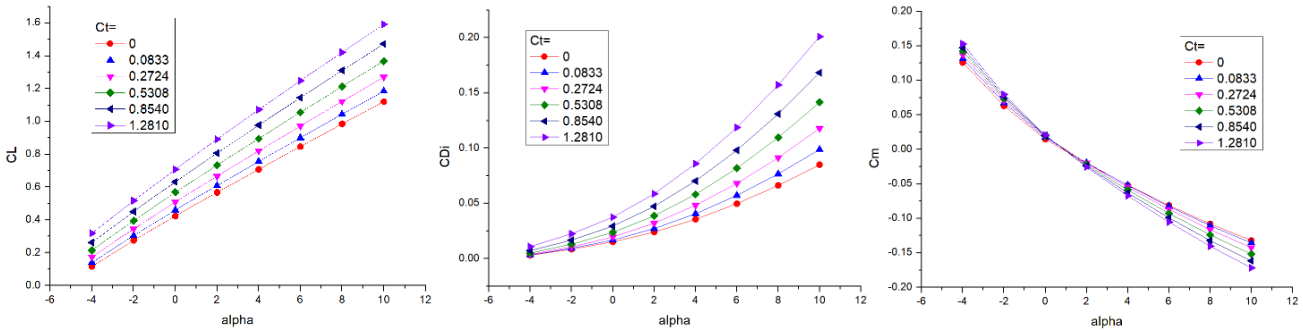


Figure 5 – Computation results of basic aerodynamic coefficients with aero-propulsive coupling.

As shown in Figure 5, at the same angle of attack, increasing the thrust coefficient C_t strengthens the propeller slipstream and significantly increases the whole-aircraft lift coefficient. At the cruise angle of attack of 2 deg, the lift coefficient increases from 0.56 to 0.90, corresponding to a 60% increase. This indicates that distributed propulsion has a significant lift-enhancement effect on the aircraft. Meanwhile, the induced-drag coefficient increases synchronously with C_t, showing that slipstream-induced lift enhancement also brings a corresponding increase in induced drag. In contrast, the pitching-moment coefficient changes only slightly. The main reason is that the aircraft uses a front-and-rear tandem-wing layout; under slipstream effects, the lift of both the front and rear wings is enhanced, and the pitching moments generated by the two wings about the center of gravity partially cancel each other. Therefore, distributed propulsion has a more direct influence on whole-aircraft lift and drag, while its influence on pitching moment depends on the combined effect of the front- and rear-wing lift increments and their relative positions with respect to the center of gravity.

Further, distributed-propulsion slipstream increases the local effective velocity and dynamic pressure over aerodynamic surfaces, thereby producing a lift increment. Under small-angle-of-attack conditions in which the slipstream direction is approximately aligned with the freestream, the lift increment in the slipstream-affected region can be approximated as:

$$C_{L,com} = \frac{V_\infty^{\,2} + v_0^{\,2}}{V_\infty^{\,2}} C_{L,base} = \left(1 + \frac{v_0^{\,2}}{V_\infty^{\,2}}\right) C_{L,base} \tag{19}$$

where v_0 is the slipstream velocity magnitude, and $C_{L,base}$ is the lift coefficient at the corresponding local angle of attack without slipstream. This shows that increasing propulsion input usually increases the local dynamic pressure and produces a positive lift increment. According to momentum theory, the slipstream induced velocity behind the propeller disk of the i-th propulsion unit can be obtained as:

$$v_0 = \frac{1}{2}\left(-V_\infty + \sqrt{V_\infty^{\,2} + \frac{2T_i}{\rho A}}\right) \tag{20}$$

where T_i is the thrust of the i-th propulsion unit and A is the propeller disk area. If differential propulsion is neglected and the thrust of each propulsion unit is assumed to be identical, namely $T = n_p T_i$, then dividing the equation by V_∞ gives:

$$\frac{v_0}{V_\infty} = \frac{1}{2}\left(-1 + \sqrt{1 + \frac{T_i}{\frac{1}{2}\rho V_\infty^2 A}}\right) = \frac{1}{2}\left(-1 + \sqrt{1 + \frac{C_t S}{n_p A}}\right) \tag{21}$$

The equation shows that, after the reference area, the number of propulsion units, and the propeller disk area are fixed, the ratio of slipstream induced velocity to freestream velocity is mainly determined by the nondimensional thrust coefficient. Therefore, a larger C_t produces a stronger increase in local dynamic pressure in the slipstream region, and the influence of distributed propulsion on whole-aircraft aerodynamic characteristics becomes more pronounced. It should be noted that local dynamic-

pressure enhancement not only changes the aerodynamic baseline values, but also amplifies aerodynamic-force responses induced by perturbations in angle of attack, angular rates, and control-surface deflections. Therefore, it further affects stability derivatives, dynamic derivatives, and control derivatives. The following analysis uses the aerodynamic derivatives associated with the propulsion state to evaluate the influence of slipstream on aircraft dynamic characteristics.

4.2 Stability and Dynamic Derivatives

The condition $\alpha = 2°$ is further selected as a representative small-angle-of-attack case. he aircraft aerodynamic derivatives are calculated for two cases: distributed propulsion off and maximum distributed propulsion on, corresponding to $C_t = 0$ and $C_t = 1.2810$, respectively. The results are shown in Table 2.

Table 2 – Calculated dynamic derivatives for "Power-Off" and "Full Power" conditions.

Derivative	Power-Off	Full Power	Derivative	Power-Off	Full Power
$C_{L\alpha}$	4.1296	6.7272	$C_{Y\beta}$	-0.2652	-0.2657
$C_{D\alpha}$	0.3127	1.3614	$C_{l\beta}$	-0.0265	-0.0332
$C_{m\alpha}$	-0.9214	-1.5063	$C_{n\beta}$	0.0750	0.0785
C_{Lq}	10.0606	15.1239	C_{Yp}	-0.0192	-0.0186
C_{Dq}	0.4885	1.7612	C_{lp}	-0.4307	-0.7606
C_{mq}	-39.0343	-61.7576	C_{np}	0.0055	0.0053
$C_{m\delta e}$	-1.3934	-2.0753	C_{Yr}	0.1819	0.1939
$C_{L\delta e}$	0.6264	0.9388	C_{lr}	0.1347	0.2023
$C_{D\delta e}$	0.0479	0.0788	C_{nr}	-0.0548	-0.0562
$C_{Y\delta r}$	0.1648	0.1650	$C_{Y\delta a}$	-0.0207	-0.0325
$C_{l\delta r}$	0.0146	0.0147	$C_{l\delta a}$	-0.0957	-0.2569
$C_{n\delta r}$	-0.0520	-0.0520	$C_{n\delta a}$	0.0060	0.0093

As shown in Table 2, after distributed propulsion is activated, the longitudinal aerodynamic derivatives exhibit significant variations. In particular, the lift-curve slope $C_{L\alpha}$, pitching-moment slope $C_{m\alpha}$ and pitch-damping derivative C_{mq} how relatively large changes. The slipstream increases the local dynamic pressure over the wing, resulting in a 63% increase in the lift-curve slope $C_{L\alpha}$. This is because a larger lift increment is generated under the same angle-of-attack perturbation, leading to a marked increase in $C_{L\alpha}$. Meanwhile, due to the redistribution of lift over the front and rear wings, the sensitivity of the overall pitching moment to the angle of attack is also enhanced, as reflected by the increase in the absolute value of $C_{m\alpha}$. For the dynamic derivatives, the distributed propulsion slipstream increases the local dynamic pressure and lift-curve slope of the wing, thereby amplifying the additional lift increment associated with the same pitch rate q. Correspondingly, the pitch-damping moment induced by the distribution of this additional lift is further enhanced, leading to an increase in the absolute value of C_{mq}. This contributes to an increase in the damping ratio of the short-period mode and attenuates the pitching oscillation response.

For the lateral-directional aerodynamic derivatives, the side-force derivative $C_{y\beta}$ changes only slightly, indicating that distributed propulsion has a relatively limited direct influence on the lateral force characteristics of the aircraft. In contrast, the derivatives associated with rolling and yawing moments vary more significantly. The slipstream induced by distributed propulsion strengthens the differential lift between the left and right wings caused by p, r, and β, thereby increasing the rolling moment and the related aerodynamic derivatives. In particular, the increase in C_{lp} indicates enhanced roll damping, which accelerates the convergence of the roll subsidence mode.

In summary, the influence of distributed propulsion slipstream on the aerodynamic derivatives of the aircraft exhibits clear directional and component-dependent characteristics. In the longitudinal direction, it is mainly manifested as enhancements in lift characteristics, pitch static stability, pitch damping, and elevator effectiveness. In the lateral-directional direction, it is primarily reflected in the enhancement of roll damping and aileron control effectiveness. These results indicate that, if the effects of distributed propulsion on aerodynamic and control derivatives are neglected in flight-dynamics modeling, it will be difficult to accurately capture the true dynamic response characteristics of the aircraft under low-speed powered conditions.

4.3 Stability Analysis

To further analyze the influence of propeller slipstream on the trim characteristics of the aircraft, a level-flight condition with $V = 10m/s$ and $\gamma = 0°$ is selected. The trim results are calculated for two cases, namely with the distributed propulsion slipstream deactivated and activated. The corresponding thrust coefficients are $C_t = 0$ and $C_t = 1.2810$, respectively, as shown in Table 3.

Table 3 – Trim calculation results with and without slipstream.

State	$\alpha(°)$	$\gamma(°)$	$V(m/s)$	$\delta_e(°)$	δ_t
Without slipstream	10.02	0	10	-3.85	0.3110
With slipstream	9.417	0	10	-3.38	0.3205

Table 3 shows that, at the same flight speed, turning on the distributed-propulsion slipstream reduces the trim angle of attack from 10.02 deg to 9.42 deg. Because the UAV lift coefficient increases under distributed propulsion, the trim angle of attack is smaller with slipstream. However, because drag also increases under slipstream effects, the throttle setting increases as well. The longitudinal and lateral-directional characteristic roots are then calculated and listed in Table 4 and Table 5.

Table 4 – Calculated longitudinal characteristic roots with and without slipstream.

State	Root1	Root2	Root3	Root4
Without slipstream	-6.5162+1.2262i	-6.5162-1.2262i	-0.117+1.119i	-0.117-1.119i
With slipstream	-10.7333	-3.6679	-0.247+0.6862i	-0.247-0.686i

Because this UAV uses a tandem-wing layout, its pitch-damping derivative is relatively large. Without slipstream, the short-period damping of the UAV is 0.983. Under the influence of propeller slipstream, the pitch-damping derivative increases significantly, and the short-period characteristic roots change from a pair of complex conjugate roots to two real roots on the negative real axis, indicating an overdamped short-period mode. The propeller slipstream also significantly increases drag and reduces the lift-to-drag ratio, so the phugoid-mode damping is larger with slipstream. It should be noted that Table 4 corresponds to the propulsion level at the trim condition, where the throttle and thrust coefficient are lower than those in the full-power derivative comparison in Table 2. Therefore, the modal changes are smaller than the maximum slipstream influence reflected by the full-power derivative changes.

Table 5 – Calculated lateral-directional characteristic roots with and without slipstream.

State	Root1	Root2	Root3	Root4
Without slipstream	0.3466	-0.838-2.893i	-0.838+2.893i	-5.9172
With slipstream	0.3571	-0.858-2.726i	-0.858+2.726i	-8.2891

Under the influence of distributed propulsion, the roll-damping derivative C_{lp} of the UAV increases, leading to a faster convergence of the roll subsidence mode. The frequency and damping of the Dutch-roll mode are mainly associated with the yaw-damping derivative and the directional static-stability derivative. Since these two derivatives show only slight differences between the cases with and without slipstream for the UAV considered in this study, the differences in the Dutch-roll frequency and damping remain generally within 10%. The stability condition for the spiral mode is $\bar{L}_\beta \bar{N}_r - \bar{L}_r \bar{N}_\beta > 0$. Although the magnitudes of $C_{l\beta}$ and C_{lr} both increase, their increments are comparable; therefore, the spiral mode remains weakly divergent. The corresponding characteristic roots change only slightly, and the time constant of the spiral mode differs little between the cases with and without slipstream.

4.4 Controllability Analysis

As shown in Table 2, $C_{m\delta e}$ is significantly enhanced under slipstream, increasing by 49% relative to the no-slipstream condition. Meanwhile, when slipstream is considered, the absolute value of $C_{l\delta a}$ increases from 0.0957 to 0.2569, and aileron roll-control effectiveness increases by approximately 168%, indicating a significant enhancement of roll-control capability. This shows that propeller slipstream not only improves the basic lift characteristics of the aircraft, but also significantly increases the local dynamic pressure in the region of the control surfaces, thereby improving both longitudinal and lateral-directional control authority. Based on these results, this paper further analyzes the influence of distributed propulsion on controllability from two aspects: aileron roll control and

propulsion-based pitch control.

4.4.1 Enhancement of Aileron Roll-Control Capability by Distributed-Propulsion Slipstream

To analyze the influence of distributed-propulsion slipstream on aileron control response, a linear state-space model is established based on the trim condition in Table 3. Lateral-directional dynamic responses with and without slipstream are then calculated under a -15 deg aileron step input. The results are shown in Figure 6.

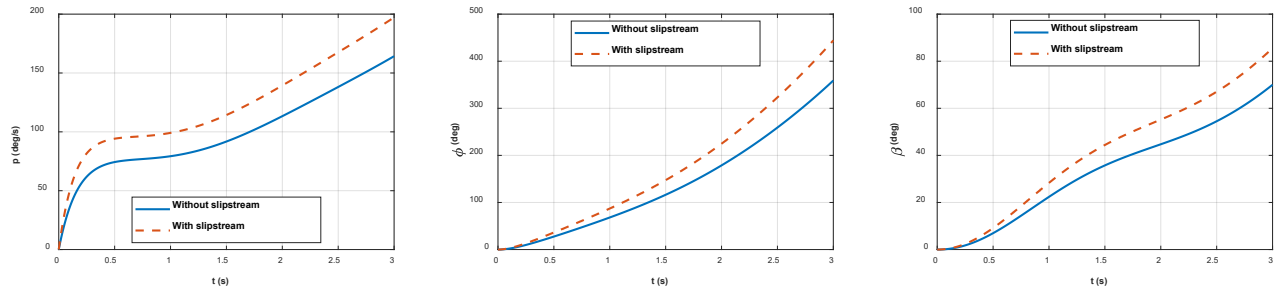


Figure 6 – Comparison of roll responses to aileron step input with and without slipstream.

Figure 6 shows that, under the same aileron input, the roll-rate, roll-angle, and sideslip-angle responses of the aircraft are all larger with slipstream than without slipstream. The roll-rate response increases most significantly, indicating that distributed-propulsion slipstream substantially improves aileron control effectiveness. This is because propeller slipstream increases the local inflow velocity and local dynamic pressure near the aileron, amplifying the additional lift increment produced by aileron deflection and thereby increasing the rolling moment generated by the aileron.

4.4.2 Enhancement of Pitch-Control Capability by Distributed Propulsion

In addition to enhancing control-surface effectiveness, the distributed-propulsion system itself can also generate additional pitching moment through slipstream-induced lift variation and thrust-line offset. For the tandem-wing distributed-propulsion aircraft studied in this paper, the front- and rear-wing propulsion units have different longitudinal and vertical positions relative to the center of gravity. When the propulsion system operates, propeller slipstream changes the lift distribution on the front and rear wings, thereby changing the whole-aircraft pitching moment. At the same time, the offset between the thrust line and the center of gravity directly generates an additional pitching moment. Therefore, the pitch-control capability of this type of aircraft comes not only from the elevator, but is also closely related to the distributed-propulsion layout and power-allocation strategy.

To further analyze the influence of front- and rear-wing distributed propulsion on pitching moment, four representative propulsion conditions are set: no power, front-wing propulsion only, rear-wing propulsion only, and simultaneous front- and rear-wing propulsion. The lift coefficient and pitching-moment coefficient under different propulsion combinations are compared in Figure 7.

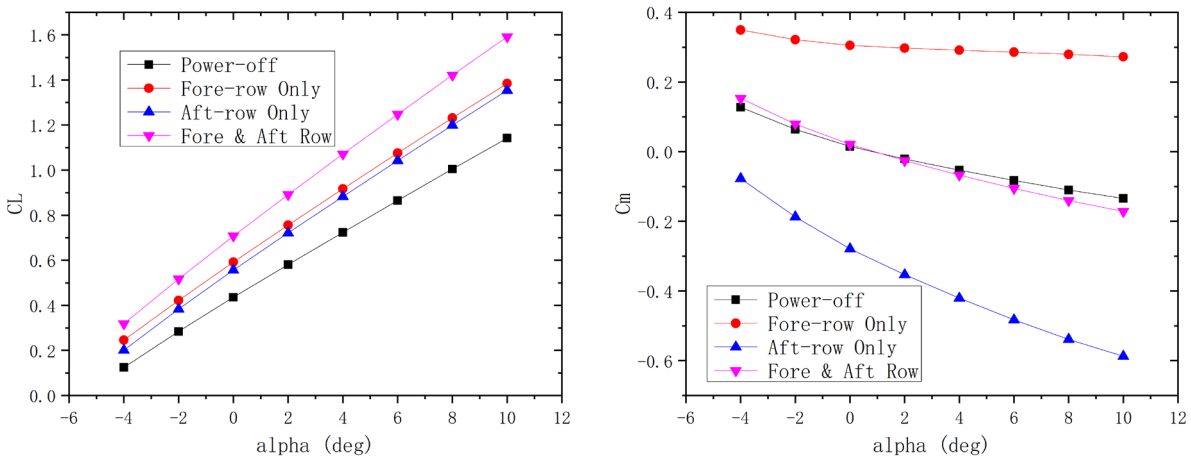


Figure 7 – Lift and Pitching Moment Coefficients Under Different Propulsion Configurations.

As shown in Figure 7, under the condition of $\alpha = 2°$, the maximum difference in C_m caused by the lift-enhancement discrepancy between the slipstreams over the front and rear wings reaches 0.65. The additional pitching moment induced by the height offset between the front and rear propulsion units and the center of gravity is approximately 0.26. Under the combined effect of these two contributions, the total increment in the pitching moment coefficient caused by distributed propulsion/aerodynamic coupling can reach 0.91. Based on an equivalent conversion using elevator pitch control effectiveness, this increment corresponds approximately to an elevator deflection of 25° under slipstream-enhanced conditions, or 37° under no-slipstream conditions. These results indicate that the distributed propulsion system can provide substantial additional pitch control capability during low-speed flight.

5. Conclusion

To address the problem that slipstream significantly affects the aerodynamic and flight-dynamic characteristics of distributed-propulsion UAVs, this paper proposes a rapid BEMT-VLM-based aero-propulsive coupling calculation method and establishes a flight-dynamics analysis model that accounts for slipstream effects. The following conclusions are obtained from a tandem-wing distributed-propulsion UAV configuration case study.

(1) A rapid distributed propulsion/aerodynamic coupling analysis method based on BEMT and VLM is established. The method can describe the influence of propeller slipstream on whole-aircraft aerodynamic forces and moments. Compared with CFD results, the errors in the main aerodynamic coefficients remain within 10%, satisfying the requirements for rapid aerodynamic-parameter acquisition and preliminary dynamic-characteristic evaluation in the conceptual design stage.

(2) Distributed-propulsion slipstream significantly changes the local dynamic pressure and effective angle of attack of the wing, thereby affecting the whole-aircraft aerodynamic baseline values and key stability derivatives. The case-study results show that, under a representative cruise condition, slipstream increases the lift coefficient by 60%, indicating that the slipstream lift-enhancement effect can significantly change the longitudinal aerodynamic characteristics of the aircraft.

(3) The slipstream effect significantly alters the control derivatives and dynamic derivatives. The case study results show that the aileron control effectiveness increases by 168%, indicating that the distributed-propulsion slipstream can increase the local flow velocity over the control surfaces and enhance lateral control capability. Meanwhile, variations in aerodynamic derivatives such as $C_{m\alpha}$, $C_{l\beta}$, $C_{n\beta}$, C_{mq}, C_{lp}, and C_{nr} further affect the longitudinal and lateral-directional dynamic responses.

(4) Modal analysis based on the linearized state-space model shows that, under the analyzed propulsion state, slipstream increases the damping ratios of the longitudinal short-period and phugoid modes, and accelerates the decay of the lateral-directional roll-convergence mode. The proposed method enables integrated rapid evaluation of slipstream-field calculation, aerodynamic-derivative extraction, flight-dynamics modeling, and modal-characteristic analysis, and can support stability-and-control analysis of distributed-propulsion aircraft in the conceptual design stage.

6. Contact Author Email Address

Yue Zhu (zhuyue020305@mail.nwpu.edu.cn)

Rui Wang (wangrui@nwpu.edu.cn)

Yuhang Xie (yuhangxie@mail.nwpu.edu.cn)

Zhou Zhou (zhouzhou@nwpu.edu.cn)

7. Copyright Statement

The authors confirm that they, and/or their company or organization, hold copyright on all of the original material included in this paper. The authors also confirm that they have obtained permission, from the copyright holder of any third party material included in this paper, to publish it as part of their paper. The authors confirm that they give permission, or have obtained permission from the copyright holder of this paper, for the publication and distribution of this paper as part of the ICAS proceedings or as individual off-prints from the proceedings.

References

[1] Kim H D, Perry A T and Ansell P J. A review of distributed electric propulsion concepts for air vehicle technology. *2018 AIAA/IEEE Electric Aircraft Technologies Symposium*, Cincinnati, OH, United States, 2018.

[2] Khan W and Nahon M. Development and validation of a propeller slipstream model for unmanned aerial

vehicles. *Journal of Aircraft*, Vol. 52, No. 6, pp 1985-1994, 2015.

[3] Nederlof R. *Improved modeling of propeller-wing interactions with a lifting-line approach: investigation of a suitable correction method to account for the finite slipstream height*. Delft University of Technology, 2020.

[4] Long T. *An experimental investigation of propeller blown-flap airfoils*. Massachusetts Institute of Technology, 2021.

[5] Viken J K, Viken S A, Deere K A, et al. Design of the cruise and flap airfoil for the X-57 Maxwell distributed electric propulsion aircraft. *35th AIAA Applied Aerodynamics Conference*, Denver, CO, United States, 2017.

[6] Hoogreef M F M, de Vries R, Sinnige T, et al. Synthesis of aero-propulsive interaction studies applied to conceptual hybrid-electric aircraft design. *AIAA SciTech 2020 Forum*, Orlando, FL, United States, 2020.

[7] Borer N K, Derlaga J M, Deere K A, Carter M B, Viken S, Patterson M D, Litherland B and Stoll A. Comparison of aero-propulsive performance predictions for distributed propulsion configurations. *55th AIAA Aerospace Sciences Meeting*, Grapevine, TX, United States, 2017.

[8] Cheng Z Y, Yang Y X, Lu J C, et al. Effect of power layout on aerodynamic performance of distributed electric propulsion aircraft. *Acta Aerodynamica Sinica*, Vol. 42, No. 05, pp 81-96, 2024.

[9] Vechtel D and Buch J-P. Aspects of yaw control design of an aircraft with distributed electric propulsion. *CEAS Aeronautical Journal*, Vol. 13, No. 4, pp 847-860, 2022.

[10] He Z H, Kou P, Liang B H, et al. Model predictive control for power yaw of distributed electric propulsion aircraft considering slipstream effect. *Acta Aeronautica et Astronautica Sinica*, Vol. 46, No. S1, pp 166-181.

[11] Hoogreef M F M and Soikkeli J S E. Flight dynamics and control assessment for differential thrust aircraft in engine inoperative conditions including aero-propulsive effects. *CEAS Aeronautical Journal*, Vol. 13, No. 3, pp 739-762, 2022.

[12] You S, Kou P, Yao X Y, et al. Nonlinear dynamic inversion control for power yaw of distributed electric propulsion aircraft. *Journal of Aerospace* Power, Vol. 39, No. 02, pp 161-175, 2024.

[13] Tian Y, Kou P, Yao X Y, et al. Modeling and analysis of slipstream effect in the power yaw process of distributed electric propulsion aircraft. *Journal of Aerospace Power*, Vol. 40, No. 08, pp 181-193, 2025.

[14] Freeman J L and Klunk G T. Dynamic flight simulation of spanwise distributed electric propulsion for directional control authority. *2018 AIAA/IEEE Electric Aircraft Technologies Symposium*, Cincinnati, OH, United States, 2018.

[15] Botta L. *Modeling and identification of a distributed electric propulsion demonstrator aircraft*. Master's thesis, Politecnico di Milano, 2022.

[16] Cacciola S, Botta L, Riboldi C E D, et al. Identification of the impact of blowing on the aerodynamic model of an airplane with distributed electric propulsion. *34th Congress of the International Council of the Aeronautical Sciences*, Florence, Italy, 2024.

[17] Geng Y S, Zhao Y and Geng J Z. Analysis of lateral-directional flight characteristics of turboprop aircraft under strong slipstream effect. *System Simulation Technology*, Vol. 18, No. 01, pp 32-35+45, 2022.

[18] Courtin C, Hansman R J and Drela M. Flight test results of a subscale Super-STOL aircraft. *AIAA SciTech 2020 Forum*, Orlando, FL, United States, 2020.